

PAPER • OPEN ACCESS

Microwave surface transport in narrow-bandgap PdSe₂-MOSFETs

To cite this article: R Le Goff *et al* 2021 *2D Mater.* **8** 035035

View the [article online](#) for updates and enhancements.



PAPER

Microwave surface transport in narrow-bandgap PdSe₂-MOSFETs

OPEN ACCESS

RECEIVED
12 January 2021REVISED
19 April 2021ACCEPTED FOR PUBLICATION
6 May 2021PUBLISHED
24 May 2021

Original Content from
this work may be used
under the terms of the
[Creative Commons
Attribution 4.0 licence](#).

Any further distribution
of this work must
maintain attribution to
the author(s) and the title
of the work, journal
citation and DOI.

R Le Goff^{1,*}, M Rosticher¹, Y Peng², Z Liu³ , T Taniguchi⁴, K Watanabe⁴ , J-M Berroir¹, E Bocquillon¹, G Fève¹, C Voisin¹, J Chazelas⁵, B Plaçais^{1,*} and E Baudin^{1,*} ¹ Laboratoire de Physique de l'École normale supérieure, ENS, Université PSL, CNRS, Sorbonne Université, Université de Paris, 24 rue Lhomond, Paris 75005, France² State Key Laboratory of Optoelectronic Materials and Technologies, School of Materials Science and Engineering, Sun Yat-sen University, Guangzhou 510275, People's Republic of China³ CINTRA UMI CNRS/NTU/THALES, Singapore, 637553, Singapore⁴ Advanced Materials Laboratory, National Institute for Materials Science, Tsukuba, Ibaraki 305-0047, Japan⁵ THALES Def Mission Syst, F-78851 Elancourt, France

* Authors to whom any correspondence should be addressed.

E-mail: romaric.le.goff@phys.ens.fr, bernard.placais@phys.ens.fr and emmanuel.baudin@phys.ens.fr**Keywords:** PdSe₂, transistor, microwave, MOSFET, photodetectionSupplementary material for this article is available [online](#)**Abstract**

Group-10 transition-metal dichalcogenides are puckered van der Waals semiconductors, with a narrow bandgap, envisioned for ultra-broadband infrared (IR) detection. To assess their dynamical transport properties we investigate PdSe₂ n-MOSFETs by using microwave admittance spectroscopy. We report on surface channel inversion-depletion-accumulation behaviors with a depletion length of 15 nm, a mobility of 110 cm² V⁻¹ s⁻¹, and a bulk bandgap of 0.15 eV. Our 10 μm long devices have an electronic cut-off frequency in the GHz range promising a large gain-bandwidth product, competitive with that of III–V (InAs) and II–VI (HgCdTe) devices. The integration of bulk absorption and surface readout in PdSe₂-MOSFETs is a monolithic geometry suitable for fast IR detection in the application-rich 1–10 μm range, which includes molecular spectroscopy, atmospheric communications and thermal sensing.

1. Introduction

Beyond the mostly investigated group-6 transition-metal dichalcogenides (TMDs; MoS₂, MoSe₂, WSe₂) [1, 2], noble-metal-based group-10 TMDs (PtSe₂, PdSe₂, PdTe₂) have recently attracted attention due to their high carrier mobility and thickness-dependent bandgap, inherited from their puckered 2D pentagonal structure [3]. As a representing member, PdSe₂ is air-stable, easily exfoliated, and theoretically possesses an indirect bandgap of 1.3 eV in single layers that vanishes in few-layers and bulk crystals [4–6]. The transport band gap of bulk PdSe₂ is largely unknown experimentally: recent studies have estimated an optical band gap on the order of 0.5 eV [7], contrasting with ab initio predictions for the electronic band gap smaller or on the order of 0.2 eV [4, 6]. With respect to 3D semiconductors used for IR detection, the predicted bandgap is smaller than that of InAs (0.354 eV) and comparable with that of HgCdTe ternary alloys (0.1–0.3 eV). Among van der Waals materials, PdSe₂ photo-transistors

can be regarded as semiconducting alternatives to semimetallic graphene photodetectors [8], including mid-infrared (IR) photo-transistors [9] and near-IR photo-mixers [10]. The predicted PdSe₂ bandgap is demarcated by a valence band whose maximum lies at the Γ point, and a conduction band whose minimum lies in the vicinity of the S point, both bands are characterized by an effective mass $m_c^* \sim 0.2m_0$ [11]. Alike PtSe₂ [12] or PdTe₂ [13] phototransistors, few-layer PdSe₂ field-effect transistors (FETs) have been investigated, showing a large mobility $\mu > 100$ cm² V⁻¹ s⁻¹ [4, 5], and a broadband photoresponse from visible to the near infrared (NIR) range [7, 14]. Remarkably, the photoresponse can be extended to the long-wavelength mid-infrared (MIR) range in quasi-bulk samples [15, 16]. PdSe₂ mobility remains impurity limited and likely to improve with progress in material growth up to phonon-limited values [11]. Large among TMDs, it cannot surpass that of narrow bandgap semiconductors ($\sim 30\,000$ cm² V⁻¹ s⁻¹ in [17]). We show here that it is sufficient to secure a GHz electronic response. The ultra broadband optical

gain, in the wavelength range 0.4–8 μm [15, 16], and the large NIR gain $G_{\text{NIR}} \sim 700 \text{ A W}^{-1}$ [15], when combined with a large electronic bandwidth, are assets of bulk PdSe₂ photo-transistors [18]. In this work, we provide a comprehensive study of electronic transport of PdSe₂ transistors.

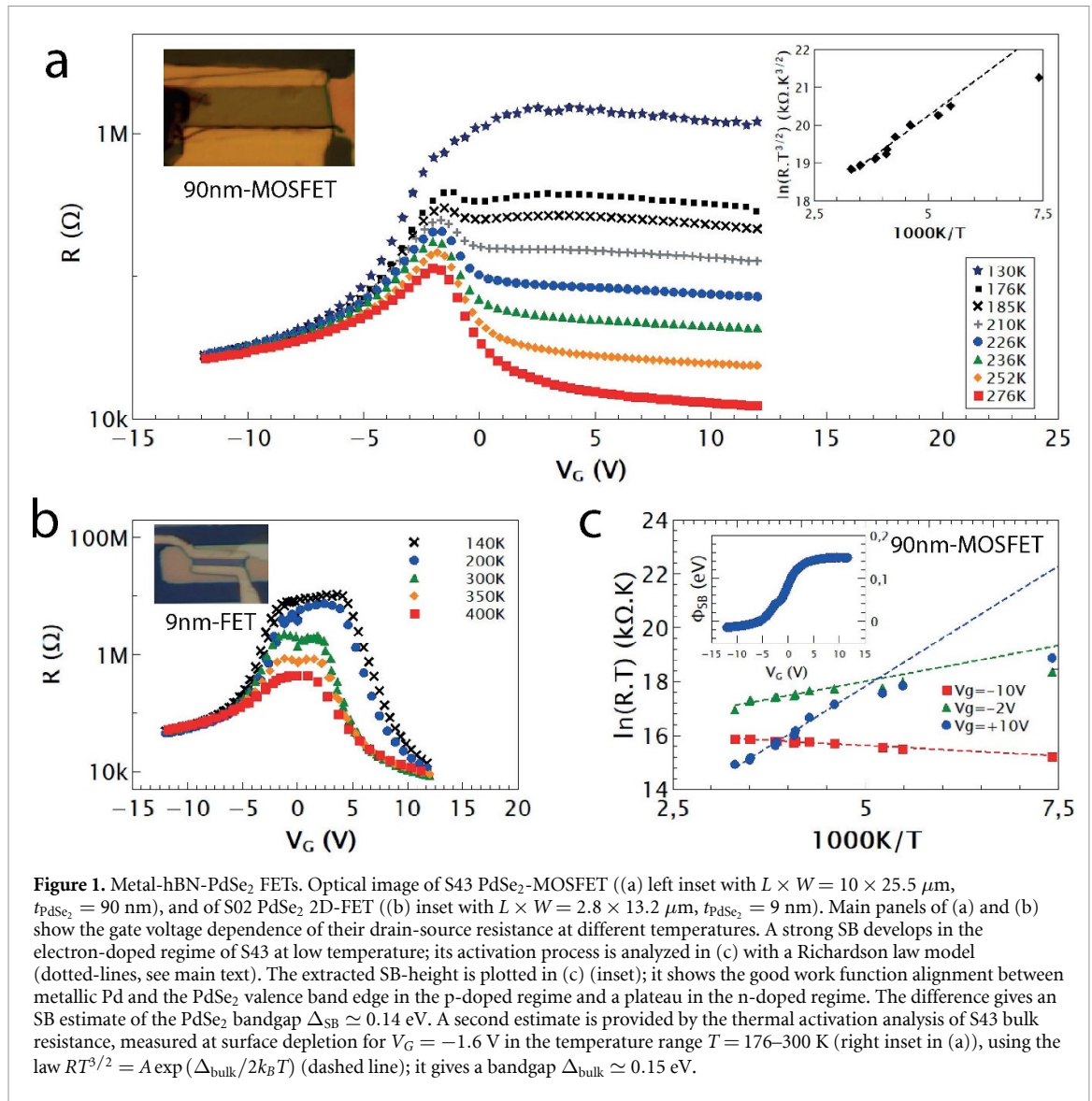
Specifications for a fast and broadband IR photo-transistor include: a narrow band gap material of sufficient thickness, wavelength compatible device dimensions, and a fast photo carrier collection and detection. High-mobility MOSFETs fulfill these constraints in combining a quasi-intrinsic bulk absorption with an efficient charge collection in the surface layer followed by a fast diffusion to the contacts. The latter mechanism limits their electronic cut-off frequency and photo-detection speed. We study Metal-hBN-PdSe₂ transistors. Due to bulk screening, DC transport in thick PdSe₂ (thickness $t_{\text{PdSe}_2} \gtrsim 100 \text{ nm}$) is qualitatively different from that of few layers conventional (unscreened) PdSe₂ 2D-FET devices ($t_{\text{PdSe}_2} \lesssim 20 \text{ nm}$) with a conductivity that vanishes in the bandgap. The thick PdSe₂ transistors are candidate MOSFETs⁶ which are van der Waals variants of conventional 3D semiconducting MOSFETs with a surface-layer dominated transport [17], and a semi-conducting bulk. Compared to conventional few layer PdSe₂ 2D-FETs, PdSe₂ MOSFETs benefit both from the more efficient absorption of incoming light by the bulk material, and from the natural protection of the conducting buried surface layer from the environment. In this letter we focus on the low-bias electronic characterization of bulk PdSe₂-MOSFETs, equipped with low Schottky-barrier (SB) Pd contacts [19], and compare them with few-layer transistors. PdSe₂-MOSFETs exhibit ambipolar transport, ensured by either p-type or n-type electrostatic doping regimes, separated by a channel depletion regime; that we define in the following with respect to an estimated residual bulk n-type doping as the characteristic surface inversion-depletion-accumulation regimes. This ambipolarity is partially warped towards low temperatures with the emergence of Schottky-contacts in the (n-doped) accumulation regime. From the thermal-activation analysis of the bulk conductance at surface depletion and of the SB resistance, we obtain two consistent estimates, $\Delta_{\text{bulk}} = 0.14 \pm 0.01 \text{ eV}$ and $\Delta_{\text{SB}} = 0.15 \pm 0.01 \text{ eV}$, of PdSe₂-MOSFET transport bandgap. These estimates contrast with the band gap value reported by literature ($\Delta_{\text{bulk}} \simeq 0.5 \text{ eV}$) [5, 7], essentially based on optical techniques, presaging dominant photon absorption mechanisms different from the indirect fundamental electronic band gap absorption. Dynamical transport properties are characterized by microwave admittance spectroscopy, which is a broad-band (100 kHz to 10 GHz) variant of standard semiconductor gate capacitance techniques

[19]. Note that high-frequency characterization of PdSe₂ 2D-FETs is precluded by the large channel resistance in depletion regime. Thanks to efficient SB capacitive coupling, microwave measurements allow overcoming SB-resistance and revealing the ambipolar channel conductance and field-effect gate capacitance of PdSe₂-MOSFETs as function of doping and temperature. The resistance-peak gate voltage V_{CNP} indicates a small bulk n-doping, corresponding to a donor density $N_D \lesssim 10^{17} \text{ cm}^{-3}$, presumably due to residual Se vacancies, which is a general trend in the literature on dichalcogenides [20]. However, in the series described in supplementary informations (available online at stacks.iop.org/2DM/8/035035/mmedia) section 2 (figure S2, panel c), three samples show no noticeable bulk doping and two samples shows a small bulk p-doping. The large electron and hole mobilities, $\mu_e \simeq 110 \text{ cm}^2 \text{ V}^{-1} \text{ s}^{-1}$ and $\mu_h \simeq 40 \text{ cm}^2 \text{ V}^{-1} \text{ s}^{-1}$, secure a GHz bandwidth in our ten-micrometer-long n-MOSFETs suited for IR sensing. The capacitance-voltage $C_G(V_G)$ dependence confirms the MOSFET inversion-depletion-accumulation regimes and allows measuring the depletion-layer thickness $\delta_{\text{dep.}} \simeq 15 \text{ nm}$. This value puts on quantitative basis the above distinction between 2D-FETs and MOSFETs based on DC transport. Finally the potential of PdSe₂-MOSFETs for fast IR detection is discussed.

2. Device fabrication and setup

PdSe₂ transistors are fabricated by exfoliating high-quality PdSe₂ crystals [4] grown by a self-flux method as described in [4], and transferring them onto large hBN flakes, exfoliated from high-quality hBN crystals grown under high pressure-high temperature as described in [21] acting as bottom-gate dielectric. Incipient to the stamping technique, the hBN thickness varies from device to device as specified in the supplementary informations (table S1 in section SI2). Transistors are deposited on a gold bottom gate itself evaporated on SiO₂ substrate. They are embedded in 50 Ω coplanar wave guides (CPW) used for DC and RF characterization. Note that this RF-device geometry precludes 4-terminal DC transport measurement and direct separation of channel and contact resistance. PdSe₂ samples are chemically etched, when needed, to the final rectangular dimensions (length $L \lesssim 10 \mu\text{m}$ and width $W \gtrsim 10 \mu\text{m}$) and equipped with low-resistance palladium (Pd) contacts using laser lithography and e-beam evaporation. The bottom gate is made of gold, which has a work function ($\mathcal{W}_{\text{Au}} = 5.3 \pm 0.2 \text{ eV}$) close to that of Pd contacts ($\mathcal{W}_{\text{Pd}} = 5.4 \pm 0.2 \text{ eV}$) [23] and of PdSe₂ valence band edge ($\mathcal{W}_{\text{PdSe}_2} = 5.4 \text{ eV}$) [3, 24]. Devices show a year-long stability, in spite of the absence of top capping. PdSe₂ structural quality is assessed by Raman spectroscopy, exemplified in figure SI1-a, with peaks

⁶ Literally MISFETs as the hBN gate insulator is not an oxide.



associated with optical phonon inelastic scattering at $\hbar\Omega_{\text{OP}} \simeq 145 \text{ cm}^{-1} = 18 \text{ meV}$ [4, 5, 25].

We have investigated two series of transistors qualified as thin ($t_{\text{PdSe}_2} \lesssim 20 \text{ nm}$) and thick ($t_{\text{PdSe}_2} \gtrsim 90 \text{ nm}$). We focus here on one representative thick device (sample S43) shown in the inset of figure 1(a), with $t_{\text{PdSe}_2} = 90 \text{ nm}$ ($t_{\text{hBN}} = 34 \text{ nm}$). Statistical relevance of S43 is illustrated in figures SI2(a–d) according to the room-temperature transfer characteristics and typical RF admittance spectra of the thick device series. For comparison, we show in the inset of figure 1(b) one representative thin device (sample S02) with $t_{\text{PdSe}_2} = 9 \text{ nm}$ ($t_{\text{hBN}} = 47 \text{ nm}$). Their micrometer sizes, specified in the caption of figure 1, match IR wavelengths. Devices are characterized in a cryogenic DC-40 GHz probe station, their RF scattering parameters being measured over a 5-decade (70 kHz to 40 GHz) bandwidth with a vector network analyzer (Anritsu-MS4644B). Thru-lines and dummy structures are used for CPW and stray capacitance de-embedding purposes. From the full set of scattering parameters we extract the device

admittance matrix, including the zero-bias gate-source contribution of interest for the physical characterization of MOSFETs [22].

3. Direct current characterization

As seen in figures 1(a) and (b), S43 and S02 devices show ambipolar transport at room temperature with similar resistances at large (positive and negative) doping, and a resistance maximum at a charge neutrality point (CNP) $V_{\text{CNP}} \sim -1 \text{ V}$. The similarity of resistances in thin (S02) and thick (S43) doped PdSe₂-transistors already suggests prominent screening effects in bulk samples. The temperature-independent CNP shift indicates a small (n-type) bulk doping. The resistance of thin S02 in figure 1(b) eventually saturates at $10 \text{ M}\Omega$ at channel depletion, due to the limited resolution of our setup.

The overall shapes of the transfer characteristics of S43 are qualitatively different. They show plateaus at positive gate voltage and low temperature

(figure 1(a)) that we attribute to the buildup of a SB at the PdSe₂-Pd interface due to work function mismatch between the Pd contact and the conduction band of PdSe₂. This barrier is elusive at negative gate voltage, confirming the good alignment between the work functions of metallic Pd and bulk PdSe₂. The transfer characteristic of S43 also shows a maximum at $V_g \simeq -1.6$ V for $T \gtrsim 150$ K, signaling the suppression of surface transport at surface charge neutrality; its temperature dependence is used below to estimate the bulk bandgap of PdSe₂. Below 150 K the Schottky contact resistance dominates over bulk resistance (see the 130 K curve in figure 1(a)), blurring the resistance maximum and precluding its quantitative analysis in terms of bulk thermal activation.

To quantify SB effects in S43, we show in figure 1(c) an activation plot together with high-temperature fits (dashed lines) with the Richardson law [26]:

$$R \times T = \frac{4\pi^2 \hbar^3}{e^2 k_B m_e^* \mathcal{A} D} \exp \frac{\Phi}{k_B T}, \quad (1)$$

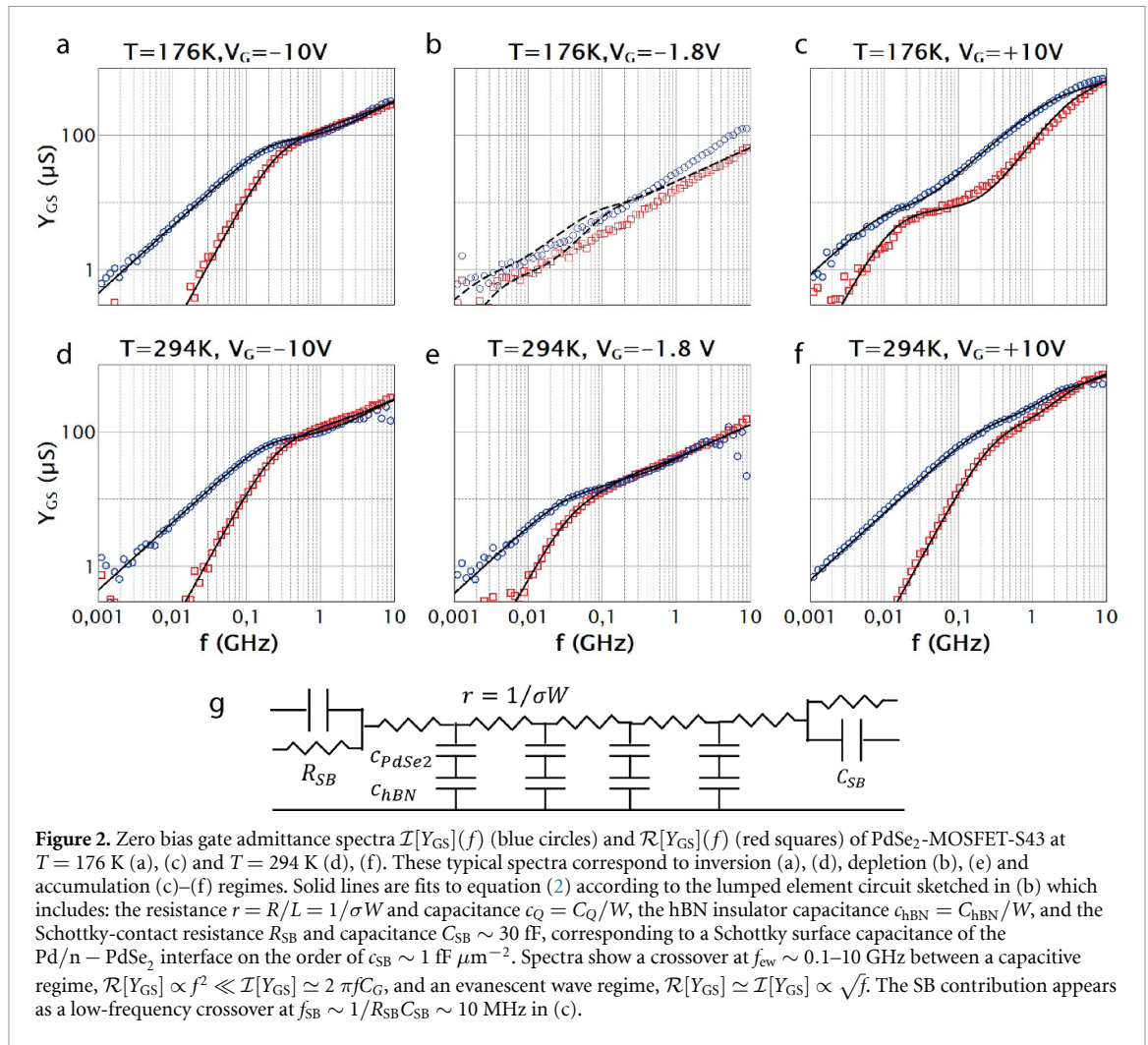
where Φ the SB height, \mathcal{A} an effective contact area, and $D < 1$ an electronic transmission factor accounting for wave-function mismatch between metallic Pd and PdSe₂. Note that a factor 2 has been introduced for the additive source and drain contributions. As seen in figure 1(c), the resistance obeys equation (1) above 100 K and saturates below presumably due to quantum tunneling. The high-temperature extrapolate, $\ln(R_{[k\Omega]} T_{[K]}) \sim 13$ (at $V_G = +10$ V), agrees with the prefactor in equation (1) taking $\mathcal{A} \sim 0.1 \mu\text{m}^2$ and $D \sim 0.01$. From the slope we extract $\Phi(V_g)$, plotted in the inset of figure 1(c), which shows a step-wise increase from $\Phi_{\text{inv}} \simeq -0.02$ eV in the inversion regime to $\Phi_{\text{acc}} \simeq +0.15 \pm 0.01$ eV in the accumulation regime (blue squares). The small negative SB extracted in the inversion regime is physically irrelevant and discloses the absence of SB between metallic Pd and p-PdSe₂. From the sum $\Phi_{\text{acc}} + \Phi_{\text{inv}}$ we infer a first estimate of PdSe₂ bandgap: $\Delta_{\text{SB}} \sim (\Phi_{\text{acc}} + \Phi_{\text{inv}}) \simeq 0.15 \pm 0.01$ eV.

We have also performed an analysis of activated transport at depletion ($V_g \simeq -1.6$ V) using the standard law for intrinsic bulk semiconductors, $RT^{3/2} = A \exp(\Delta_{\text{bulk}}/2k_B T)$. The analysis is limited to a reduced temperature range $T = 150\text{--}300$ K where a the resistance peak at surface charge neutrality is visible, securing a negligible contribution of contact SB effects. We deduce an estimate of the bandgap $\Delta_{\text{bulk}} = 0.15$ eV. A similar analysis performed on S02 yields a somewhat larger $\Delta_{\text{bulk}} \simeq 0.3$ eV. This blueshift of the electronic band gap is in line with the band gap value of 0.57 eV for a slightly thinner PdSe₂ flake (6.8 nm-thick) reported in Ref. [7], also based on an Arrhenius plot. These values remain below the ultimate theoretical expectation $\Delta \simeq 1.3$ eV for single layer PdSe₂. Based on these two independent determinations, we

conclude that transport bandgap of semi-bulk PdSe₂ does not completely vanish but rather saturates at $\Delta_{\text{PdSe}_2} = 0.15$ eV, consistently with theoretical prediction in [4]. Note that while the SB is used here for bandgap characterization purpose, it can be minimized by appropriate contact engineering [27] for applications.

4. High-frequency admittance spectroscopy

Field-effect capacitance is a well established characterization technique of semiconductor devices [19]. It can be performed in capacitors (MOSCAPs) or transistors (MOSFETs). MOSCAPs are commonly made of silicon [28], or narrow-bandgap InAs [29] semiconductors, with a top gate and a thin oxide insulator, distinctively called MOS devices. The gate capacitance is generally measured between the top gate and the (weakly) doped bulk. Here we use an in-plane variant of admittance spectroscopy for a long channel transistor geometry, taking into account the Schottky contact impedance. This variant is similar to previous capacitor modeling that has been introduced for gate capacitance spectroscopy to study graphene electronic compressibility [22] and used to characterize high-mobility hBN-encapsulated graphene devices (including plasma-resonant capacitors) [30], the topological Dirac states at the surface of Bi₂Se₃-tetradymites [33, 34], the interface states of topological heterojunctions between normal and inverted HgTe/CdHgTe semiconductors [31], as well as the edge states of strained HgTe quantum wells [32]. The complex gate-source admittance is measured over a broad frequency range allowing for a combined in-situ characterization of gate capacitance $C_G(V_G)$ and channel conductivity $\sigma(V_G)$. For ideal carrier injection in the channel, the admittance spectrum reflects a crossover from an elastance ($1/C_G$) dominated regime at low frequency to a lattice-friction dominated regime at high frequency. Such an RF crossover from elastic-dominated to friction-dominated response is quite general and has been previously reported in the context of vortex matter dynamics in superconductors [35–37]. In atomically thin 2D materials, screening is negligible and one can readily extract from C_G the quantum compressibility contribution $C_Q = e^2 \text{DOS}$ in series with the geometrical capacitance C_{geo} . This provides in turn a determination of the chemical potential $E_F = \int (C_G/C_{\text{geo}} - 1) dV_g$ and the diffusion constant $D = \sigma/C_Q$, yielding a genuine scattering spectroscopy encoded in the $D(E_F)$ dependence [31]. For massive PdSe₂ carriers, the 2D density of states in the surface layer, $\text{DOS} = m^*/\pi \hbar^2 \sim 10^{14} \text{ cm}^{-2} \text{ eV}^{-1}$, is large such that $C_Q \gg C_{\text{geo}}$, and the gate-voltage dependence of C_G mostly stems from series dielectric channel contributions. These contributions read



$C_{PdSe_2} \approx \epsilon_{PdSe_2}/\delta_{dep/inv}$, with δ_{dep} the depletion-layer depth at neutrality, and δ_{inv} that of the $p^+ - n$ junction in the inversion regime.

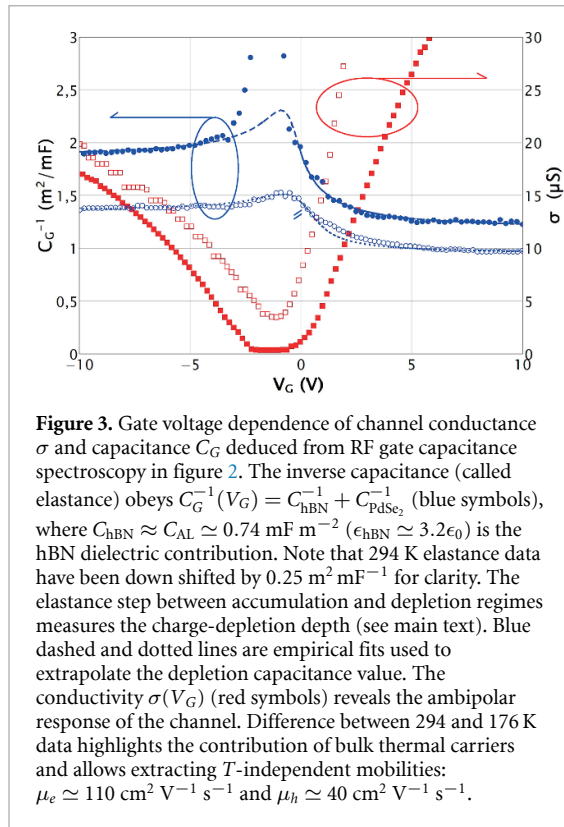
Figure 2 shows typical RF admittance spectra of the PdSe₂ n-MOSFET S43. The gate admittance $Y_{GS}(\omega) = Y_{12}(\omega)$ is reported both at room temperature $T = 294$ K (d)–(f) and low temperature $T = 176$ K (a,c). Negative and positive gate voltages correspond to (hole) inversion and (electron) accumulation regimes. A room-temperature depletion spectrum, for $V_g \sim -1$ V, is shown in panel (e). Also shown in the figures are theoretical fits with a 1D charge diffusion model [22, 32] based on a lumped-element description (sketched in figure 2(b):

$$Y_{GS}(\omega) = \frac{1 - e^{-\gamma L}}{Z_D + Z_0} \frac{1 + \Gamma_S \exp -\gamma L}{1 - \Gamma_D \Gamma_S \exp -2\gamma L}, \quad (2)$$

where $Z_0 = \sqrt{\frac{r}{j\epsilon_g \omega}}$ and $\gamma = \sqrt{jrc_g \omega}$ are the line impedance and propagation constant respectively, with $r = R/L$ and $c_g = C_g/L$ the resistance and gate capacitance per unit length. Z_S and Z_D are the source and drain contact impedance, and $\Gamma_D = \frac{Z_D - Z_0}{Z_D + Z_0}$, $\Gamma_S = \frac{Z_S - Z_0}{Z_S + Z_0}$ are the reflection coefficients at the drain and source contact respectively. The contact impedance

is modeled as $Z_{SB} = (R_{SB}^{-1} + jC_{SB}\omega)^{-1}$ and the channel conductivity is $\sigma = (rW)^{-1}$. As seen in figures 2(a, c–f), the 1D-model (solid lines) captures well the 4-decades admittance spectra, both at room temperature (d–f) and in the inversion/accumulation regimes at low temperature (a,c). It fails describing the low- T depletion regime in figure 2(b) when both surface-layer and bulk transport are suppressed. Similarly, it also fails describing S02 admittance spectra for most of the doping range (not shown). The 1D response is characterized by a crossover frequency $f_{ew}(V_G) \sim 1$ GHz between a low-frequency capacitive regime, $\mathcal{I}(Y_{GS}) \propto f$ and $\mathcal{R}(Y_{GS}) \propto f^2$, and a high-frequency regime, $\mathcal{R}(Y_{GS}) \simeq \mathcal{I}(Y_{GS}) \propto f^{1/2}$, which is characteristic of evanescent waves in diffusive media. In the depletion regime (figure 2(e)), f_{ew} drops to a finite 0.1 GHz value controlled by the small, thermally activated, bulk conduction. The transport crossover frequency f_{ew} acts as a cutoff frequency for photo-transistors above which photo-carrier detection is limited to the very vicinity of contacts, within a length $\text{Re } \gamma^{-1} \ll L$.

Using a model fitting for each gate bias point (see the supplementary videos for $T=176$ K and $T=300$ K), we perform somehow a "radiography" of



the MOSFET and we extract the deembedded contact and channel resistances. In supplementary informations (section 3), they are analyzed with the same Richardson and Arrhenius plots used in DC (see section 3). Both analyses confirm a bandgap value of 0.15 eV and the consistency of DC and RF responses.

But we can now push our analysis further, by extracting accurate values of gate capacitance $C_G(V_G)$ and channel resistivity $\sigma^{-1}(V_G)$, as shown in figure 3. At room temperature, the contact impedance Y_{SB}^{-1} is reduced and Y_{GS} is mostly dominated by the channel contribution. The situation is different at low-temperature, specifically in the accumulation regime ($V_G > 0$), where contact resistance was shown to be overwhelming at DC (see figure 1(a)). Its signature is a low-frequency deviation from the 1D propagation, below a SB cutoff frequency $f_{\text{SB}} \sim 1/R_{\text{SB}}C_{\text{SB}} \sim 10 \text{ MHz}$. Above f_{SB} , the large contact resistance ($R_{\text{SB}} \sim 1 \text{ M}\Omega$), opaque to DC, is bypassed by the contact capacitance ($C_{\text{SB}} \sim 30 \text{ fF}$) and one recovers a diffusive channel admittance response. A proper account of R_{SB} and C_{SB} in equation(2) allows extracting reliable values of C_G and σ . By deembedding contact contributions, figure 3 illustrates the temperature effect on the channel elastance $1/C_G = 1/C_{\text{hBN}} + 1/C_{\text{PdSe}_2}(V_G)$ and the ambipolar conductivity.

Let us focus first on the room-temperature data (empty symbols) in figure 3. Channel conductivity (empty red squares) depicts, with an enhanced precision compared to the DC data in figure 1(a), the ambipolar character and the strong gate modulation of the PdSe₂-MOSFET. It peaks at $\sigma^{-1} \approx 280 \text{ k}\Omega$

in the depletion regime ($V_g \approx -0.7 \text{ V}$), and drops down to $\sigma^{-1} \approx 5 \text{ k}\Omega$ in the accumulation regime ($V_g = +10 \text{ V}$), and $\sigma^{-1} \approx 50 \text{ k}\Omega$ in the inversion regime ($V_G = -10 \text{ V}$). Carrier mobility is fair, with $\mu_{\text{acc.}} \approx 110 \text{ cm}^2 \text{ V}^{-1} \text{ s}^{-1}$ and $\mu_{\text{inv.}} \approx 40 \text{ cm}^2 \text{ V}^{-1} \text{ s}^{-1}$, approaching the $\mu \approx 250 \text{ cm}^2 \text{ V}^{-1} \text{ s}^{-1}$ value reported in PdSe₂ FETs after annealing [4, 5]. Gate elastance (blue circles, note that data are shifted by $-0.25 \text{ m}^2 \text{ mF}^{-1}$ for clarity) is characteristic of n-MOSFETs [19, 28, 29]: it saturates in the accumulation regime at the (nominal) gate insulator value $C_G \approx C_{\text{hBN}} \approx 0.74 \text{ mF m}^{-2}$, takes a minimum $C_G \approx 0.52 \text{ mF m}^{-2}$ at depletion, and increases to a plateau $C_G \approx 0.56 \text{ mF m}^{-2}$ characteristic of an inversion regime [19]. From the additivity of insulator ($1/C_{\text{hBN}}$) and semiconductor ($1/C_{\text{PdSe}_2}$) elastance contributions, we deduce $C_{\text{PdSe}_2} \approx 1.75 \text{ mF m}^{-2}$ at depletion and $C_{\text{PdSe}_2} \approx 2 \text{ mF m}^{-2}$ in the inversion regime. Relying of the theoretical estimate $\epsilon_{\text{PdSe}_2} = 3\epsilon_0$ [38], we infer $\delta_{\text{dep}} \approx 15 \text{ nm}$ and $\delta_{\text{inv}} \approx 13 \text{ nm}$. These small screening lengths, which are consistent with the Debye length $L_D = \sqrt{k_B T \epsilon_{\text{PdSe}_2} / e^2 N_D} \gtrsim 7 \text{ nm}$ for a bulk doping $N_D \lesssim 1 \cdot 10^{17} \text{ cm}^{-3}$, secure the MOSFET interpretation of our 90 nm-thick S43 device, and justify the qualitative difference between our thin and thick transistor series.

The difference between 294 and 176 K data in figure 3 illustrates thermal effects on mobility and carrier density. As expected the capacitance gate modulation is more contrasted at 176 K due to a smaller contribution of the thermal carriers to screening. To quantify the first effect we cannot rely on direct measurement of C_G at depletion due to the above-mentioned poor quality of the fits. Instead, we have used a three-parameters empirical interpolation formula, $C_G^{-1}(V_g) = C_G^{-1}(+10 \text{ V}) - a \tanh [(V_g - V_{\text{CNP}})/b] + c / \sqrt{b^2 + (V_g - V_{\text{CNP}})^2}$ where a , b and c encode respectively for the capacitance step between depletion and accumulation, the amplitude and width of the capacitance dip at neutrality. Catching the room temperature $C_G(V_G)$ data (dotted blue line), it is used to fit 176 K data over the inversion/accumulation regimes (dashed blue line). With this procedure we infer $\delta_{\text{inv}} \approx 15 \text{ nm}$ and $\delta_{\text{dep}} \approx 20 \text{ nm}$ at 176 K. Temperature effect on $\sigma(V_G)$ is also instructive: room-temperature data are mainly upshifted by a constant amount $\Delta\sigma \approx 3 \mu\text{S}$ with respect to 176 K data, implying that: (1) the mobility is essentially T -independent as expected for impurity scattering, and (2) the bulk contribution, which is suppressed at 176 K, is thermally activated at room temperature with a bulk resistivity $t_{\text{PdSe}_2} / \Delta\sigma \approx 3 \text{ Ohm.cm}$. This value is consistent with a thermal carrier density $n_i(300 \text{ K}) \sim 1 \times 10^{17} \text{ cm}^{-3}$ for a bandgap $\Delta_{\text{bulk}} = 0.15 \text{ eV}$, and a bulk mobility $\mu_{\text{bulk}} \approx 20 \text{ cm}^2 \text{ V}^{-1} \text{ s}^{-1}$. The finite bulk mobility augurs well of a fast bulk-surface dynamics of photo-carriers under illumination as anticipated in section [1].

5. Conclusion

In this letter we have reported on low-bias DC transport and RF gate capacitance spectroscopy in high-quality PdSe₂ crystals providing qualitative and quantitative evidence that semi-bulk van der Waals PdSe₂ transistors behave as genuine narrow-bandgap MOSFETs. This extensive electronic characterization allows down-pinning relevant material parameters such as PdSe₂ work function, transport bandgap, mobility, and thermal carrier density. In particular, we have deduced a fundamental electronic bandgap of 0.15 eV in agreement with the *ab initio* studies [4, 6]. Our work suggests that the optical gap of 0.5 eV for bulk PdSe₂ reported in the literature [7] originates from higher energy transitions and offers guidance for further IR optoelectronic applications, in particular for MIR detection. Finite bias properties (not reported here) confirm the quasi-intrinsic quality of our PdSe₂ transistors. However they call for a different out-of-equilibrium physics (phonon-induced velocity saturation, self heating, etc) which is beyond the scope of the present paper.

The demonstration of PdSe₂-MOSFETs opens new perspectives for applications of 2D materials in high-speed optoelectronics including ultra broadband optical detectors covering the MIR range. The present demonstration of GHz electronic bandwidth at the MIR-relevant 10 μm length scale, put in perspective with literature photo-detection measurements of an optical gain $G = 700 \text{ A W}^{-1}$ [15], opens an avenue to PdSe₂ MOSFETs for room-temperature monolithic broadband and high-speed sensing, competing the extensively used CdHgTe detectors [39].

Data availability statement


The data that support the findings of this study are available upon reasonable request from the authors.

Acknowledgments

Authors acknowledge fruitful discussions with A Vasanelli and Y Guldner and thank M Pala for proofreading the manuscript before submission. The research leading to these results has received partial funding from the European Union 'Horizon 2020' research and innovation programme under Grant Agreement No. 881603 'Graphene Core', from the ANR-2018-CE08-018-05 'BIRDS'. R Le Goff thanks Thales Systèmes Aéroportés for the CIFRE Grant No. 2016/1294 funding.

ORCID iDs

Z Liu  <https://orcid.org/0000-0002-8825-7198>

K Watanabe  <https://orcid.org/0000-0003-3701-8119>

B Plaçais  <https://orcid.org/0000-0003-2408-7393>

E Baudin  <https://orcid.org/0000-0003-3694-9640>

References

- [1] Wang Q H, Kalantar-Zadeh K, Kis A, Coleman J N and Strano M S 2012 Electronics and optoelectronics of two-dimensional transition metal dichalcogenides *Nat. Nanotechnol.* **7** 699
- [2] Schwierz F, Pezoldt J and Granzner R 2015 Two-dimensional materials and their prospects in transistor electronics *Nanoscale* **7** 8261
- [3] Rasmussen F A and Thygesen K S 2015 Computational 2D materials database: electronic structure of transition- metal dichalcogenides and oxides *J. Phys. Chem. C* **119** 13169
- [4] Chow W L *et al* 2017 High mobility 2D palladium diselenide field-effect transistors with tunable ambipolar characteristics *Adv. Mater.* **29** 1602969
- [5] Oyedele A D *et al* 2017 PdSe₂: pentagonal two-dimensional layers with high air stability for electronics *J. Am. Chem. Soc.* **139** 14090
- [6] Sun J, Shi H, Siegrist T and Singh D J 2015 Electronic, transport and optical properties of bulk and mono-layer PdSe₂ *Appl. Phys. Lett.* **107** 153902
- [7] Zhang G *et al* 2019 Optical and electrical properties of two-dimensional palladium diselenide *Appl. Phys. Lett.* **114** 253102
- [8] Koppens F H L, Mueller T, Ph A A, Ferrari C, Vitiello M S and Polini M 2014 Photodetectors based on graphene, other two-dimensional materials and hybrid systems *Nat. Photon.* **9** 780
- [9] Huang P *et al* 2020 Ultra-long carrier lifetime in neutral graphene-hBN van der Waals heterostructures under mid-infrared illumination *Nature Commun.* **11** 863
- [10] Hamidouche L, Montanaro A, Rostischer M, Poupet B, Taniguchi T, Watanabe K, Plaçais B, Baudin E and Legagneux P 2021 Opto-electronic mixing in high mobility graphene *ACS Photon.* **8** 369
- [11] Qin D, Yan P, Ding G, Ge X, Song H and Gao G 2018 Monolayer PdSe₂: a promising two-dimensional thermoelectric material *Sci. Rep.* **8** 2764
- [12] Yu X *et al* 2018 Atomically thin noble metal dichalcogenide: a broadband mid-infrared semiconductor *Nature Comm.* **9** 1545
- [13] Guo C *et al* 2020 Anisotropic ultrasensitive PdTe₂-based phototransistor for room-temperature long-wavelength detection *Sci. Adv.* **6** eabb6500
- [14] Di Bartolomeo A *et al* 2019 Pressure-tunable ambipolar conduction and hysteresis in ultrathin palladium diselenide field effect transistors *Adv. Func. Mater.* **29** 1902483
- [15] Liang Q *et al* 2019 High-performance, room temperature, ultra broadband photodetectors based on air stable PdSe₂ *Adv. Mater.* **31** 1807609
- [16] Zeng L-H *et al* 2019 Controlled synthesis of 2D palladium diselenide for sensitive photodetector applications *Adv. Funct. Mater.* **29** 1806878
- [17] Lin Y C, Yamaguchi H, Chang E Y, Hsieh Y C, Ueki Y M, Hirayama Y and Chang C Y 2007 Growth of very-high-mobility AlGaSb/InAs high-electron-mobility transistor structure on Si substrate for high speed electronic applications *Appl. Phys. Lett.* **90** 023509
- [18] Sorger V J and Maiti R 2020 Roadmap for gain-bandwidth-product enhanced photodetectors: opinion *Opt Mater Express* **10** 2192
- [19] Hu C C 2009 *Modern Semiconductor Devices for Integrated Circuits* 1st edn (New Jersey: Pearson) p 351
- [20] Liu X *et al* 2021 Temperature-sensitive spatial distribution of defects in PdSe₂ flakes (arXiv: 2104.06642)
- [21] Taniguchi T and Watanabe K 2007 Synthesis of high-purity boron nitride single crystals under high pressure by using Ba-BN solvent *J. Cryst. Growth* **303** 525

- [22] Pallecchi E, Betz A C, Chaste J, Fève G, Huard B, Kontos T, Berroir J-M and Plaçais B 2011 Transport scattering time probed through rf admittance of a graphene capacitor *Phys. Rev. B* **83** 125408
- [23] Lide R 2008 CRC handbook of chemistry and physics *J. Am. Chem. Soc.* **130** 1
- [24] Liu X, Zhou H, Yang B, Qu Y and Zhao M 2017 Strain-modulated electronic structure and infrared light adsorption in palladium diselenide monolayer *Sci. rep.* **7** 39995
- [25] Puzosky A A, Oyedele A D, Xiao K, Haglund A V, Sumpter B G, Mandrus D, Geoghegan D B and Liang L 2018 Anomalous interlayer vibrations in strongly coupled layered PdSe₂ *2D Mater.* **5** 035016
- [26] Richardson O W 1901 On the negative radiation from hot platinum *Phil. Camb. Phil. Soc.* **11** 286
- [27] Oyedele A D *et al* 2019 Defect-mediated phase transformation in anisotropic two-dimensional PdSe₂ crystals for seamless electrical contacts *J. Am. Chem. Soc.* **141** 22, 8928
- [28] Lo S-H, Buchanan D A and Taur Y 1999 Modeling and characterization of quantization, polysilicon depletion and direct tunneling effects in MOSFETs with ultrathin oxides *IBM J. Res. Dev.* **43** 327
- [29] Wang S-W *et al* 2015 Field-effect mobility of InAs surface channel nMOSFET with low dit scaled Gate-Stack *IEEE Trans. Elec. Dev.* **62** 2429
- [30] Graef H *et al* 2018 Ultra-long wavelength Dirac plasmons in graphene capacitors *J. Phys. Mater.* **1** 01LT02
- [31] Inhofer A *et al* 2017 Observation of Volkov–Pankratov states in topological HgTe heterojunctions using high-frequency compressibility *Phys. Rev. B* **96** 195104
- [32] Dartailh M C *et al* 2020 Dynamical separation of bulk and edge transport in HgTe-based 2D topological insulators *Phys. Rev. Lett.* **124** 076802
- [33] Inhofer A *et al* 2018 RF-quantum capacitance of topological insulator Bi₂Se₃ in the bulk depleted regime for field-effect transistors *Phys. Rev. Appl.* **9** 024022
- [34] Inhofer A *et al* 2019 RF compressibility of topological surface and interface states in metal-hBN-Bi₂Se₃ capacitors *J. Phys. Mater.* **2** 04400
- [35] Plaçais B, Mathieu P, Simon Y, Sonin E B and Traito K B 1996 Continuum electrodynamics of type-II superconductors in the mixed state: the dc and ac response *Phys. Rev. B* **54** 13083
- [36] Lütke-Entrup N, Plaçais B, Mathieu P and Simon Y 1997 Depinning transition in type-II superconductors *Phys. Rev. Lett.* **79** 2538
- [37] Lütke-Entrup N, Plaçais B, Mathieu P and Simon Y 1998 RF-studies of vortex dynamics in isotropic type-II superconductors *Physica B* **255** 75
- [38] Deng S, Li L and Zhang Y 2018 Strain modulated electronic, mechanical and optical properties of the monolayer PdS₂, PdSe₂ and PtSe₂ for tunable devices *ACS Appl. Nano Mater.* **1** 1932
- [39] Gravrand O, Mollard L, Boulade O, Moreau V, Sanson E and Destefanis G 2012 Ultralow-dark-current CdHgTe FPAs in the SWIR range at CEA and sofradir *J. Electron. Mater.* **41** 2686